Research article

JGS
Journal of the Geological Society

https://doi.org/10.1144/jgs2024-021 | Vol. 181 | 2024 | jgs2024-021

Using U–Pb carbonate dating to constrain the timing of extension and fault reactivation within the Bristol Channel Basin, SW England

Joe Connolly[1*], Mark Anderson[1], Catherine Mottram[2], Gregory D. Price[1], Randall Parrish[2] and David Sanderson[3]

[1] School of Geography, Earth and Environmental Sciences, University of Plymouth, Plymouth PL4 8AA, UK
[2] School of the Environment, Geography and Geosciences, University of Portsmouth, Portsmouth PO1 2UP, UK
[3] Department of Ocean and Earth Sciences, University of Southampton, Southampton SO17 1BJ, UK
JC, 0009-0006-7740-593X; MA, 0000-0001-8058-2271; CM, 0000-0002-5664-1259
* Correspondence: Joe_Connolly97@outlook.com

Abstract: The Bristol Channel Basin is a Mesozoic continental rift basin. The basin is an important analogue for offshore reservoirs. Relative cross-cutting relationships and correlation with adjacent sedimentary basins have previously been used to constrain the timing of basin development. *In situ* U–Pb carbonate geochronology has been used to date calcite slickenfibre development in the cores of normal, thrust and strike-slip faults in the East Quantoxhead and Kilve region of Somerset for the first time. Protracted north–south extension from *c.* 150 to 120 Ma formed normal faults. Subsequent north–south shortening from *c.* 50 to 20 Ma was accommodated by (1) mutually cross-cutting strike-slip faults, (2) minor east–west-striking thrust faults and (3) the reactivation of pre-existing normal faults. Throughout Cenozoic contraction, σ_2 and σ_3 remained similar in magnitude and periodically flipped to become vertical; this was probably controlled by local stress permutations and changes in fluid pressure. The timing of inversion is contemporaneous with dominant Pyrenean and later Alpine orogenic events, as well as the opening of the Mid-Atlantic Rift. Early inversion of the Bristol Channel Basin was probably driven by far-field Pyrenean deformation, with later contraction caused by Alpine forces. Ridge push from the Mid-Atlantic Rift exacerbated the reactivation of the basin.

Supplementary material: Details of analytical methods and U–Pb and geochronology data are available at https://doi.org/10.6084/m9.figshare.c.7293400

Received 31 January 2024; **revised** 5 June 2024; **accepted** 6 June 2024

Constraining the timing and duration of faulting related to basin formation and inversion is important for understanding regional tectonic frameworks and how deformation is partitioned in continental crust over time, and provides insights into fluid flow processes during deformation (e.g. Roberts and Holdsworth 2022). Understanding the timing and nature of fluid flow through fractures has implications for understanding structural trapping in hydrocarbon exploration, carbon capture and storage projects (Zhang *et al.* 2014) and fracture-controlled fluid migration in enhanced geothermal systems (Huenges 2016). In areas with multiple structural phases, the evolution of structures can vary spatially, making it difficult to establish a coherent structural framework. For example, reactivation can cause multiple slip events along structures (Stewart *et al.* 1999), and the rotation of structures and local perturbation of stress can make determining relative relationships problematic (Fossen 2016). Constraining the timing of continental rifting is essential when evaluating the maturation of a basin, as well as the impact of subsequent tectonic events.

Advances in mass spectrometry techniques have allowed for materials with very low U concentrations such as calcium carbonate (typically <5 ppm U) to be dated using *in situ* laser ablation techniques (e.g. Roberts *et al.* 2020). This has opened a wide range of possibilities for dating low-temperature faulting and fluid-flow processes, as reviewed by Roberts and Holdsworth (2022). U–Pb carbonate dating has been widely used to quantify the absolute timings of fault movement in several tectonic settings (e.g. Coogan *et al.* 2016; Roberts and Walker 2016; Parrish *et al.* 2018; Mottram *et al.* 2020; Looser *et al.* 2021; Tamas *et al.* 2022), providing the opportunity to directly date tectonic inversion across Europe.

Widespread tectonic inversion of Mesozoic rift basins across Northern Europe during the Cenozoic is important for understanding strain partitioning in the upper crust, and the impact of far-field tectonic events (Peacock and Sanderson 1999; Peacock 2009; Parrish *et al.* 2018; Rodríguez-Salgado *et al.* 2020; Blaise *et al.* 2022; Monchal *et al.* 2023). There are two main tectonic drivers responsible for basin inversion across Europe: (1) mantle plume activity, underplating and ridge push associated with opening of the Mid-Atlantic (Hallam 1971; Tiley *et al.* 2004; Williams *et al.* 2005; Barnett-Moore *et al.* 2017; Hardman *et al.* 2018; Lovell 2023); (2) the closure of the Tethys Ocean (Torfstein and Steinberg 2020), resulting in the Alpine and Pyrenean orogenic events (Vergés *et al.* 2002; De Graciansky *et al.* 2011).

Inversion structures in the Faroe–Rockall area have been attributed to ridge push from the Mid-Atlantic Ridge (Boldreel and Andersen 1993). Stress modelling conducted by Stephenson *et al.* (2020) suggested significant transmission of stress to Britain and Ireland from the opening of the Mid-Atlantic. Mantle pluming in the Paleocene is also thought to have caused uplift in the Irish Sea (Rowley and White 1998), and Cenozoic underplating (Tiley *et al.* 2004) is thought to have had a significant impact on uplift and inversion in the St Georges Channel Basin (Williams *et al.* 2005) in the Paleogene. It has also been suggested that the tilting of Thames Valley could be due to Icelandic mantle pluming (Lovell 2023).

The inversion of sedimentary basins in southern Britain and Ireland including the Wessex, Mizen and Bristol Channel basins has traditionally been attributed to far-field stresses associated with the Alpine Orogeny during the early Miocene (c. 23 Ma) (Lake and Karner 1987; Blundell 2002; Pfiffner *et al.* 2002; Peacock 2009; Rodríguez-Salgado *et al.* 2020). Pyrenean deformation is generally considered to be older, having had a more significant impact on northern Europe during the Eocene–Oligocene (c. 50–32 Ma) (Pfiffner 2002; Sinclair *et al.* 2005). U–Pb carbonate geochronology has provided absolute timing constraints for basin inversion across Europe, including in the Wessex Basin, England (Parrish *et al.* 2018), Paris Basin, France (Blaise *et al.* 2022), western Norway (Hestnes *et al.* 2023), East Irish Sea (Monchal *et al.* 2023), the Pyrenees, Spain (Cruset *et al.* 2020; Parizot *et al.* 2020, 2021) and the Jura, Switzerland (Looser *et al.* 2021; Smeraglia *et al.* 2021). Despite this wealth of recent carbonate dating studies across Europe, there remains debate around the relative significance of Cenozoic tectonic events for reactivation in southern Britain and elsewhere (Peacock 2009; Parrish *et al.* 2018; Monchal *et al.* 2023). This paper aims to provide the first U–Pb carbonate dating constraints in the Bristol Channel Basin to evaluate the relative importance of far-field stresses on basin inversion in this region.

The Bristol Channel Basin (BCB) has been selected as a site to study the evolution and reactivation of structures because of the high-quality exposure and preservation of 3D structural geometries along the basin margin in Somerset, UK. It is generally interpreted to have formed as a half-graben during the Mesozoic (Cornford 1986), and subsequently underwent uplift and contraction during the Cenozoic (Nemčok *et al.* 1995; Kelly *et al.* 1999; Peacock and Sanderson 1999; Miliorizos *et al.* 2004; Rotevatn and Peacock 2018). It has been used as an onshore analogue for basin inversion tectonics (Williams *et al.* 1989; Peacock and Sanderson 1999). The structural evolution of the BCB has been well established using relative cross-cutting and abutting relationships of fracture populations including faults, joints and veins (Peacock and Sanderson 1999; Sanderson 2016; Rotevatn and Peacock 2018).

The timing of faulting in the BCB has previously been constrained through sedimentary thickening relationships, synsedimentary deformation and comparison with similar basins elsewhere in southern Britain. For example, the timing of contraction is constrained by comparing with folding in the adjacent Wessex basin (Chadwick 1993) rather than primary evidence within the BCB itself, highlighting the need for direct constraints on faulting in the BCB. Here, U–Pb carbonate dating is used to constrain the absolute timing of fault development and reactivation in the BCB for the first time, adding direct age constraints to the established structural history.

The main objectives of this paper are to (1) structurally characterize (including microstructures) calcite veins associated with normal faults developed during basin extension, and thrust and strike-slip faults associated with later contraction or inversion, (2) obtain U–Pb ages from synkinematic calcite veins associated with different mapped faults in the Lower Lias (Early Jurassic; Fig. 1) succession of the BCB, exposed on the Somerset coast and (3) use these data to test, and quantify, hypotheses concerning the age and tectonic drivers of faulting in the BCB and elsewhere, such as the nearby Mizen Basin in the South Celtic Sea.

Geological setting of the Bristol Channel Basin

The Bristol Channel Basin (BCB) (Fig. 1) initially formed during extension in the Permian–Triassic caused by rifting associated with the break-up of Pangaea (Debenham *et al.* 2020). This led to the formation of a series of east–west-striking normal faults (Dart *et al.* 1995; Nemčok *et al.* 1995; Peacock and Sanderson 1999; Glen *et al.* 2005). The reactivation of Variscan thrust faults in the underlying pre-Permian basement (Miliorizos *et al.* 2004) is interpreted to have partly controlled the development of normal faults and may be responsible for the overall east–west structural trend of the entire basin (Dart *et al.* 1995). The most extensive exposures of Liassic (Early Jurassic) rocks on the south side of the BCB are between

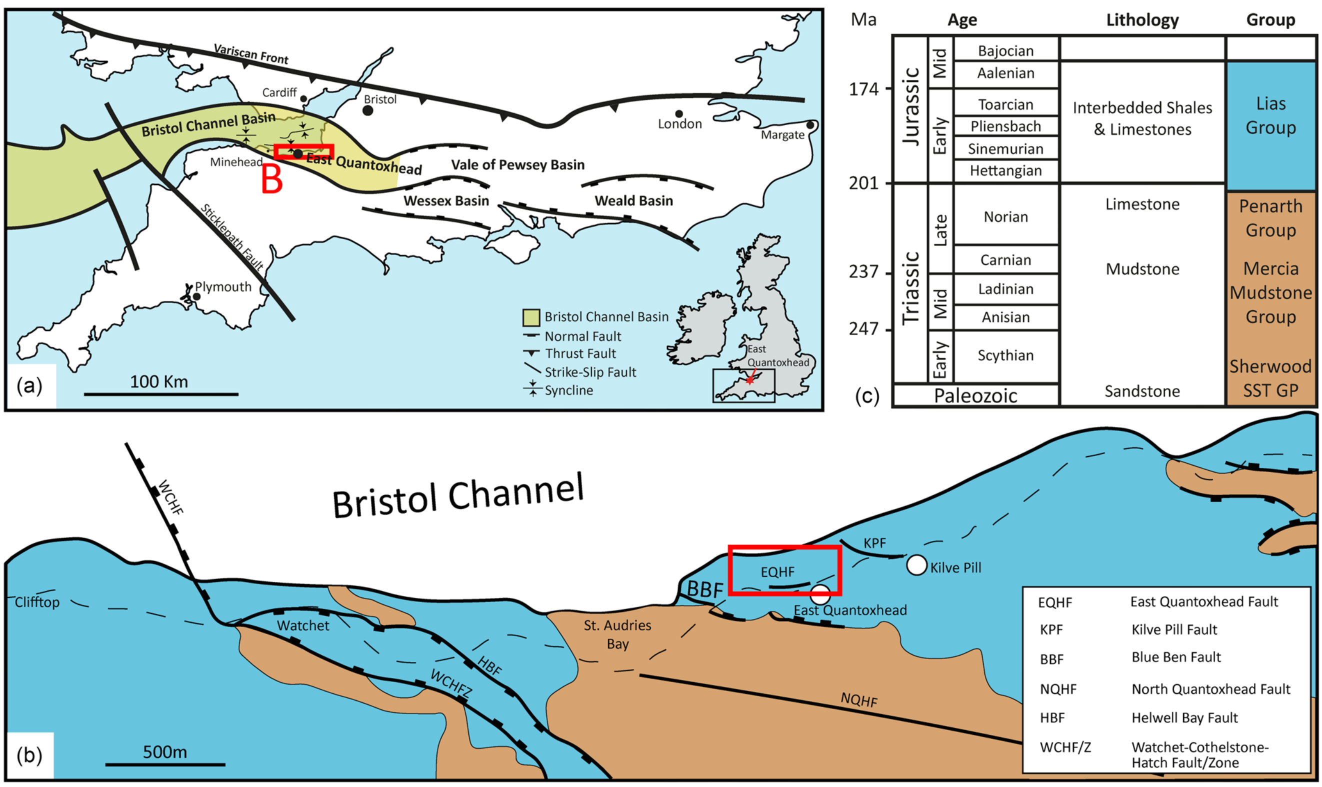

Fig. 1. Study location with fault map and simplified stratigraphy. (**a**) Key structures of SW England and the location of the Bristol Channel Basin (BCB) in relation to nearby basins. (**b**) Key structures of the North Somerset coast section of the BCB, including Kilve and East Quantoxhead, which are the focus of this study. (**c**) Stratigraphic column of the BCB Source: (a–c) after Glen *et al.* (2005).

Kilve and East Quantoxhead where they are cut by multiple fault populations, which are the focus of this study (Fig. 1). Burial estimates, based on the maturation of organic material in Liassic sedimentary rocks, suggest that maximum burial of *c.* 1.7 km and temperature of *c.* 65°C occurred during the Aptian (*c.* 125–113 Ma), with much of the Jurassic strata having been eroded during uplift from *c.* 55 Ma to the present day (Cornford 1986).

Extension

East–west-striking normal faults in the BCB (Peacock and Sanderson 1991, 1993, 1999; Dart *et al.* 1995; Nemčok *et al.* 1995; Kelly *et al.* 1999; Glen *et al.* 2005; Peacock *et al.* 2017) formed during Triassic north–south extension, under relatively low-stress conditions (*c.* 11 MPa) (Nemcok and Gayer 1996). The timing of deformation is constrained by synsedimentary deformation of the Mercia Mudstone Group (Fig. 1) (Nemčok *et al.* 1995). The normal faults formed with σ_1 subvertical and σ_3 plunging gently NNE (Peacock *et al.* 2017), consistent with the broader interpretation of north–south extension based on kinematic analysis (Nemčok *et al.* 1995; Kelly *et al.* 1999; Peacock and Sanderson 1999; Glen *et al.* 2005).

Contraction

Strike-slip faults that are conjugate about north–south (Kelly *et al.* 1998, 1999), thrust faults that crosscut normal faults (Peacock *et al.* 2017; Rotevatn and Peacock 2018) and the reactivation of pre-existing normal faults (Kelly *et al.* 1999) document a stage of contraction in the BCB that post-dates initial extension (Dart *et al* 1995; Nemčok *et al.* 1995; Kelly *et al.* 1999; Peacock and Sanderson 1999; Glen *et al.* 2005; Peacock *et al.* 2017). During the later stage of contraction, σ_1 is interpreted to have plunged gently to the south (Peacock *et al.* 2017). Reactivation is seen in normal faults with >22 m throw, such as the East Quantoxhead Fault (EQHF) and Blue Ben Fault (Kelly *et al.* 1999). This period of north–south contraction is interpreted to have occurred in the Cenozoic based on monoclinal folding in the adjacent Wessex Basin (Chadwick 1993). Inversion is also thought to have led to an increase in fluid pressure, which led to increased reactivation (Williams *et al.* 2005).

Veins as indicators of fluid flow in the Bristol Channel Basin

Veins are often used as proxies to study palaeo-fluid flow (Nemčok *et al.* 1995; Passchier and Trouw 2005; Philipp 2012; Spruženiece *et al.* 2021). The composition, distribution and position relative to other structures reveal the depth, source of fluids and opening mode of veins. Furthermore, dating of mineralization provides a tool for understanding the timing of fluid flow and interplay between fluids and the structural development of an area. Petrographical analysis of veins within the BCB shows evidence for blocky veins formed by epitaxial growth on seed grains in open fractures, which precipitated and sealed in one event (Spruženiece *et al.* 2021). Geochemical analysis of the calcite veins at Kilve yielded evidence of radiogenic alteration by radiogenic basinal fluids sourced from deeper sediments indicated by higher $^{87}Sr/^{86}Sr$ ratios (Bixler *et al.* 1998; Debenham *et al.* 2020). Oxygen and carbon isotope data show that the mineralizing fluids were 20–30°C hotter (80–110°C) than the surrounding host rocks (60–80°C) (Philipp 2012).

Methods

Sampling strategy

Prior to sampling, faults were mapped in the field and fault types were determined using slickenfibre kinematics, fault dip, bed matching and other indicators such as en echelon veins. Faults with clear kinematics (dip-slip or strike-slip) and evidence of synkinematic calcite slickenfibres were selected for sampling. Twenty-one faults were sampled across the foreshore from East Quantoxhead to Kilve beach (Tables 1 and 2; Fig. 2). Once faults were characterized, slickenfibres from the fault core were sampled and then made into thin (30 µm) and thick (80 µm) polished sections for laboratory analysis.

Fault kinematics

Fault data underwent kinematic analysis in Stereonet 11 and FaultKin8 (Marrett and Allmendinger 1990; Allmendinger 2012). Principal stress axes were determined using fault orientation data with slickenfibre pitch recorded in the field. Kinematic results have been combined with U–Pb carbonate ages where possible to determine the absolute temporal evolution of the stress field.

Microstructural evolution of calcite veins

Thin sections were used for microtextural analysis and to determine grain-size distribution and recrystallization textures in veins before U–Pb analysis was undertaken on the corresponding thick sections. Thin sections were analysed using plane- and cross-polarized light (PPL and XPL). Undulose extinction and sub-grains were used to infer, respectively, crystal plastic and recovery. Dynamic recrystallization comprised bulging (BLG), and subgrain rotation (SGR) recrystallization types (Passchier and Trouw 2005). Calcite twin type was used to determine palaeotemperature using the technique of Passchier and Trouw (2005).

Minerals within the thick sections were identified using a JEOL 7001F FE-SEM at Plymouth Electron Microscopy Centre, University of Plymouth, with an Oxford Instruments X-Max 50 mm^2 energy-dispersive spectroscopy detector and AZtec v6.0 software. Operating conditions were accelerating voltage 20 keV, probe current *c.* 6 nA and working distance 10 mm. This analysis was carried out using internal standards and with a deadtime of 35–50%.

U–Pb geochronology

Dating of synkinematic calcite slickenfibres allows for ages to be attributed to the timing of movement along a fault. *In situ* U–Pb carbonate geochronology was conducted at the University of Portsmouth by laser ablation inductively coupled plasma mass spectrometry (LA-ICP-MS). Laser ablation was conducted using an ASI RESOlution© 193 nm ArF excimer laser coupled to a high-sensitivity Jena Analytic PlasmaQuant Elite© ICP-MS (2021–22 analyses) or Agilent 8900 Triple Quadrupole ICP-MS instrument (2023 analyses). Calcite vein samples were analysed *in situ* in polished 80 µm thick polished sections. Calcite was analysed using 80 µm spot size, laser fluence of *c.* 2.5–3 J cm^{-2}, and a repetition rate of 8 Hz. NIST glasses, NIST SRM612 (NIST612; 38 ppm U and 39 ppm Pb; Jochum *et al.* 2011, for Jena ICP-MS analyses) and NIST SRM614 (NIST614; 0.8 ppb U and 2.3 ppm Pb, Jochum *et al.* 2001, for Agilent 8900 analyses) and WC-1 carbonate (254.4 ± 6.4 Ma; Roberts *et al.* 2017) were used as primary reference materials. Mudtank Zircon (732 ± 5 Ma; Black and Gulson 1978; Jackson *et al.* 2004) and Duff Brown Limestone (64 ± 2 Ma; Hill *et al.* 2016) were used as secondary reference materials to verify long-term reproducibility. Analysis of Duff Brown during the analytical period yielded a $^{206}Pb/^{238}U$ intercept age of 64.35 ± 0.6 Ma (0.54% reproducibility). Analysis of Mudtank Zircon during the analytical period yielded a $^{206}Pb/^{238}U$ intercept age of *c.* 734.7 ± 2.6 Ma (0.37% reproducibility).

U–Pb data were reduced using Iolite©3 software (Paton *et al.* 2011). Samples generally have low to very low U content (<1 ppm),

Table 1. The grain-size distribution, vein mode and deformation features present within different structures

Sample	Structure type	Evidence for reactivation	Vein structure	Primary fabric	Features	Primary grain size	Secondary grain size	Overprint textures				
								Crystal plastic			Brittle deformation	
								Undulose extinction (Y/N)	SGR (Y/N)	BLG (Y/N)	Twin type (1, 2, 3)	Brittle features
JC-15-21A	Dex ss	n	Composite	E > B	n	0.2–3.0	n.a.	Y	±	Y	±1, 2	F
JC-1C-21A	Dex ss	n	Composite	E > B	n	0.1–1.0	0.1–0.3	Y	±	±	1, 2	F
JC-1C-21B	Dex ss	n	Composite	E > B	n	0.1–1.0	0.1–0.3	Y	Y	±	1, 2	F
JC-1d-21B	Dex ss	n	Composite	E > B	n	0.1–1.2	0.1–0.3	Y	Y	±	1, 2	F
JC-6a-21	Dex ss	n	Composite	B > E	n	0.05–2.5	0.1–0.3	Y	±	±	1, 2	F
JC-9a-21	Dex ss	n	Composite	E > B	n	0.2–1.5	n.a.	Y	Y	Y	1, 2	F
JC-1a-21	Sin ss	n	Composite	E > B > F	n	0.2–2.0	n.a.	Y	±	±	1, 2	F
JC-1d-21A	Sin ss	n	Composite	B > E	n	0.2–1.2	0.2–0.04	Y	±	±	1, 2	F
JC-8-21	Sin ss	n	Composite	E > B	n	0.2–2.5	0.2–0.5	Y	±	±	1	F
JC-9b-21	Sin ss	n	Composite	B > E	n	0.1–0.06	n.a.	Y	±	±	1, 2	F
JC-4-21	Thrust	n	Composite	B > E	TG, Cr	0.2–1.5	n.a.	Y	Y	±	1, 2	F
JC-6b-21	Thrust	n	Composite	E > B	TG, Cr, F	0.2–2.0	0.1–0.3	Y	Y	±	1, 2	F
JC-18-22	Thrust	n	Composite	B	TG, Cr, F, SVJ	0.1–2.5	0.1–0.5	Y	±	Y	1, 2	F
JC-25-22	Thrust	n	Composite	E > B	Cr, SVJ	0.1–5.0	0.1–0.5	Y	±	Y	±1, 2	F
JC-10-21	Normal	n	Composite	E > B	n	0.1–3.0	0.1–0.5	Y	Y	±	1, 2	F
JC-12-21	Normal	y	Composite	B > E	n	0.1–2.2	0.1–0.5	Y	Y	±	1, 2	F
JC-5-21	Normal	n	Composite	E > B	n	0.1–3.0	0.1–0.5	Y	Y	Y	1, 2	F
JC- 16 -21	Normal	y	Composite	B	Cr	0.2–4.0	0.1–0.3	Y	Y	Y	1, 2	F
JC-13-21	Normal	y	Composite	E > B	n	0.2–2.5	0.2–0.4	Y	Y	±	1, 2	F, C
JC-14-21	Normal	n	Composite	E > B	n	0.2–2.5	0.2–0.4	Y	Y	±	1, 2	F, C
JC-3A-21	Normal	y	Single	B	n	0.1–1.5	0.1–0.4	Y	Y	±	1, 2	F
JC-3B-21	Normal	y	Single	B	n	0.2–0.7	0.1–0.3	Y	Y	±	1, 2	F
JC-3C-21	Normal	y	Single	E > B	n	0.3–0.6	0.2–0.3	Y	Y	±	1, 2	F
JC-3D-21	Normal (reactivated)	y	Single	B > E	n	0.3–1.1	0.3–0.4	Y	Y	±	1, 2	F

Primary fabric: E, elongate crystals; B, blocky crystals. Features: n, none; TG, tension gash; Cr, crenulation; F, fibres; SVJ, shear vein jog. Brittle features: F, fracturing; C, cataclastic texture. n.a., not analysed (not present). Structure types: Dex ss, dextral strike-slip fault; Sin ss, sinistral strike-slip fault; Thrust, thrust (reverse) fault; Normal, normal (extensional) fault; Normal (reactivated), normal fault with signs of reactivation. Examples of textures are shown in Figure 5.

Table 2. Sample numbers and location, showing dip/direction as well as age data calculated using Tera–Wasserburg plots

Sample	Latitude	Longitude	Dip/direction	Structure type	Age	Absolute internal error ±	Absolute propegated error ± (1%)	MSWD	*n* (spots)
JC-15-21	484326	5671296	38/000	Dex ss	21.8	0.62	0.66	1.3	58
JC-1C-21A	483391	5671110	78/262	Dex ss	29.9	2.3	2.32	1.5	39
JC-1C-21B	483391	5671110	78/263	Dex ss	31.77	3.78	3.79	0.7	59
JC-1d-21B	483391	5671110	84/120	Dex ss	34.98	1.7	1.74	1.7	120
JC-6a-21	483284	5671140	89/290	Dex ss	35.98	1.56	1.60	1	39
JC-9a-21	483288	5671071	89/270	Dex ss	34.48	2.76	2.78	0.41	60
JC-1a-21	483391	5671110	71/294	Sin ss	40.97	5.67	5.68	0.95	40
JC-1d-21A	483391	5671110	71/294	Sin ss	35.63	2.04	2.07	1.1	120
JC-8-21	483324	5671104	60/316	Sin ss	34.48	2.5	2.52	0.94	40
JC-9b-21	483288	5671071	86/104	Sin ss	39.34	4.76	4.78	0.42	40
JC-4-21	483022	5670917	35/022	Thrust	41.88	1.26	1.33	0.52	57
JC-6b-21	483284	5671140	24/274	Thrust	36.58	2.6	2.63	0.96	60
JC-18-22	482128	5670731	20/152	Thrust	41.69	5.1	5.12	0.83	58
JC-25-22	483022	5670920	20/010	Thrust	36.63	2.65	2.68	1.8	38
JC-10-21	483238	5671030	40/022	Normal	146.81	3.46	3.76	1.2	59
JC-12-21	484260	5671314	36/012	Normal	140.18	1.76	2.25	1.2	59
JC-5-21	483306	5671088	70/208	Normal	149.59	4.12	4.38	0.68	44
JC- 16 -21	484577	5671371	38/000	Normal	149.96	2.79	3.17	0.51	50
JC-13-21	484260	5671314	38/000	Normal	135.25	2.37	2.73	1.5	59
JC-14-21	484315	5671306	34/178	Normal	120.2	2	2.33	1.1	45
JC-3A-21	483022	5670917	57/178	Normal	147	10	10.11	1.1	39
JC-3B-21	483022	5670917	57/178	Normal	136.54	4.26	4.47	3.1	20
JC-3C-21	483022	5670917	57/178	Normal	116.48	4.94	5.08	3	20
JC-3D-21	483022	5670917	57/178	Normal (reactivated)	33.51	3.37	3.39	10	64

Example Tera–Wasserburg plots are shown in Figure 6.

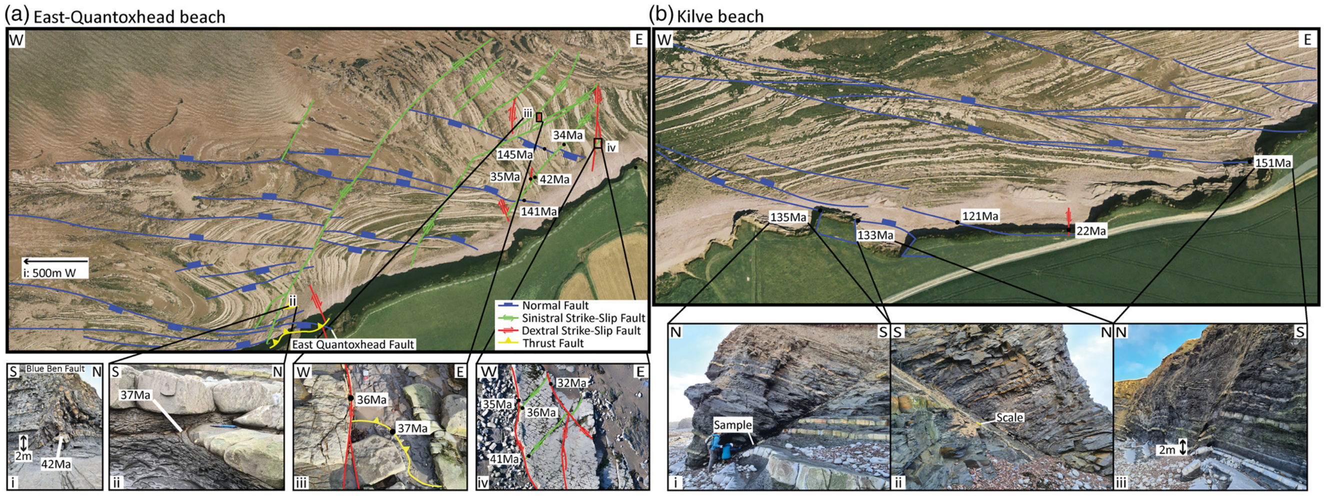

Fig. 2. (**a**) Fault map of East Quantoxhead beach. i, Thrust shortcut in Blue Ben Fault (sample 18), 42 Ma; ii, small thrust fault (sample 25), 37 Ma; iii, small-scale dextral strike-slip fault (sample 6A, 36 Ma) and small thrust fault (sample 6B, 37 Ma); iv, cross-cutting dextral and sinistral strike-slip faults (sample 1). (**b**) Fault map of Kilve beach. i, Normal fault: Kilve Pill Fault (sample 12, 140 Ma); ii, normal fault: also Kilve Pill Fault (sample 13, 135 Ma); iii, normal fault (sample 16, 150 Ma).

low Th/U ratios and have been regressed and plotted using both Tera–Wasserburg (TW) and 86TW plots (see Parrish *et al.* 2018), using IsoplotR (Vermeesch 2018). Tera–Wasserburg plots were calculated with discordia (model-1) age calculations (as displayed in the Supplementary material), and 86TW plots as isochrons with a type 1 2D regression and using model 1 (maximum likelihood) (Vermeesch 2018). Both 86TW and U–Pb plots have used 2 SE (abs) for input and output errors (see Supplementary material for more detail). In all cases, the 86TW plot has less scatter and lower uncertainties, whereas many of the samples have excess scatter using the traditional TW plot, and the 86TW ages and uncertainties are used as the final quoted ages. Final quoted 2σ uncertainties are propagated in quadrature and include fully propagated analytical uncertainties of 1% (see Supplementary material for full details). Chronostratigraphical ages are based on the International Chronostratigraphic Chart v2023/09 (Cohen *et al.* 2013, updated).

Field and microstructural observations

Extensional faults

East–west-striking normal faults are extensively exposed in the foreshore, extending hundreds of metres (Figs 2 and 3), with slips ranging from <1 to >20 m. Normal faults terminate in isolated tips, but are more commonly linked by relay zones, which may then breach to form a larger through-going fault as also noted by Peacock and Sanderson (1991, 1993). Some larger normal faults, such as the Kilve Pill Fault, East Quantoxhead Fault and Blue Ben Fault (Fig. 2), show evidence of inversion, localized thrusting and reverse fibres, and folding of the hanging wall can be observed (Figs 2 and 4). Kelly *et al.* (1999) also observed inversion features in some reactivated normal faults in the region. Normal faults dip both north and south, with dips ranging from *c.* 40 to 80°. Faults have been analysed as bulk populations, without division based on location in the field. Kinematic analysis of normal faults generated robust estimates for kinematic tensors, producing a vertical σ_1 and a horizontal σ_3, which trends broadly north–south (Fig. 3).

All studied veins within normal faults are composed of calcite (Fig. 5). The East Quantoxhead Fault (EQHF) also contains localized celestine. Normal fault calcite crystal sizes range from 0.2 to 5.0 mm. All normal faults show evidence for recrystallization and sub-grain development (Fig. 5) with sub-grain diameter ranging from 0.2 to 0.5 mm. Crystal plasticity is inferred from undulose extinction and dynamic recrystallization by sub-grain rotation (SGR), present in all samples, as well as bulging (BLG), which is present only in selected samples (Table 1). Both type 1 and 2 calcite twins are present in normal faults.

Contractional faults

NE–SW-striking sinistral strike-slip faults extend >400 m (Fig. 2), and typically have up to 10 m of lateral offset. They can be seen to cross-cut normal faults (Fig. 4). North–south-striking dextral strike-slip faults dip at *c.* 60–90° and extend for tens of metres. Dextral

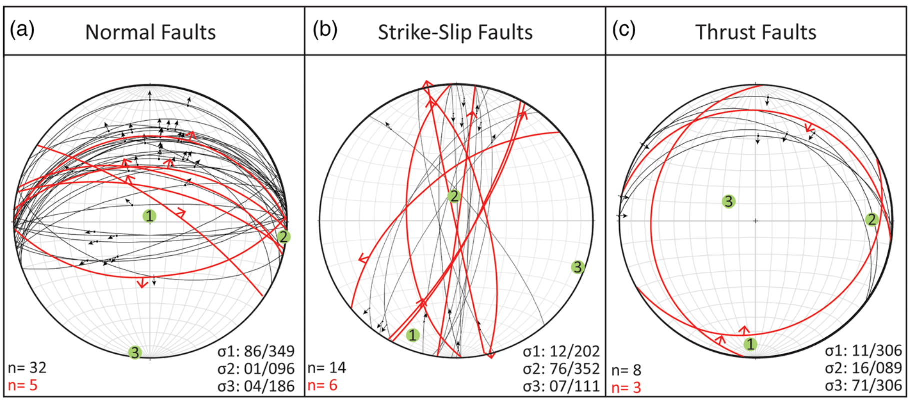

Fig. 3. Stereograms of kinematic field data for different fault populations; data from the Kilve–East Quantoxhead region. Stereogram show the estimated values for $\sigma_{1,2,3}$ based on fault dip and strike and striae trend, produced in FaultKin8. Dated faults highlighted in red. (**a**) Normal faults show a horizontal σ_3 trending north–south, and a vertical σ_1. (**b**) Strike-slip faults show a subhorizontal σ_3 trending NNE–SSW and a subvertical σ_2. (**c**) Thrust faults show a subhorizontal σ_1 trending north–south and a subvertical σ_3.Sources: Marrett and Allmendinger (1990) and Allmendinger (2012).

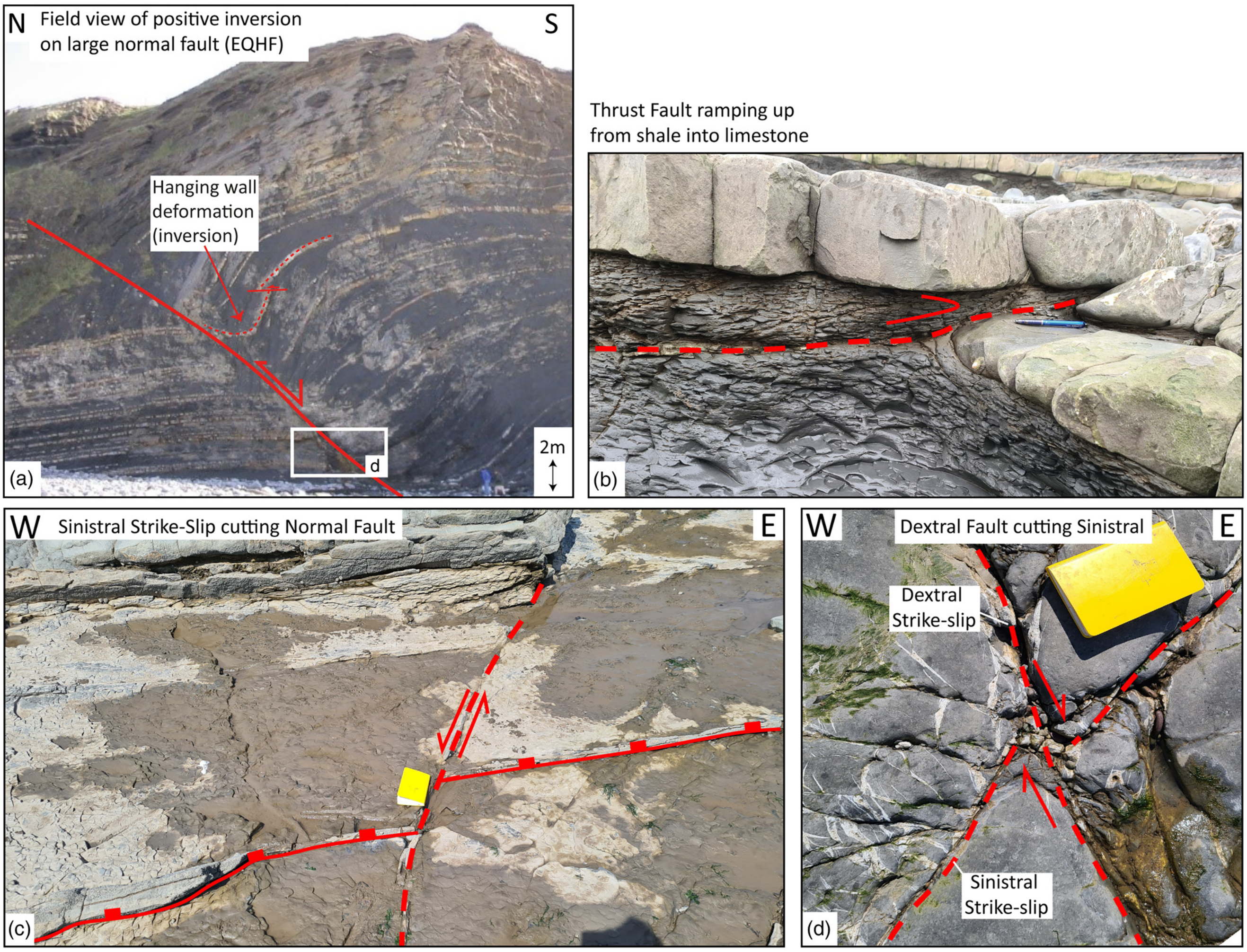

Fig. 4. Field photographs of fault relationships. (**a**) Normal fault (EQHF) striking east–west, showing evidence for hanging-wall inversion. (**b**) Small thrust fault ramping up into limestone from shale unit. (**c**) Sinistral strike-slip fault striking NE–SW cutting across east–west-trending normal fault. (**d**) North–south-striking dextral strike-slip fault cross-cutting NE–SW-striking sinistral strike-slip fault.

faults are less pervasive than sinistral ones and are not observed to offset normal faults; instead they are located between overlapping normal faults, as reported by Rotevatn and Peacock (2018). Sinistral and dextral strike-slip faults mutually cross-cut, suggesting that they are a conjugate system. Thrust faults are the least common structure; they are generally observed in mudstone lithologies proximal to reactivated normal faults (Fig. 2). East–west-striking thrust faults have small throws of between 5 and 30 cm and gentle dips ranging from *c.* 15 to 40°. Kinematic analysis of contractional features suggests a subhorizontal σ_1 that trends broadly north–south or NNE–SSW based on thrust and strike-slip data, with strike-slip faults producing a subvertical σ_2 and thrust faults producing a subvertical σ_3.

Veins

Veins associated with sinistral strike-slip faults have crystal diameters that range from 0.5 to 2.5 mm and have sub-grain diameters ranging from 0.2 to 0.5 mm, with two of four samples showing evidence for sub-grain development. Dextral strike-slip fault vein crystal diameters range from 0.05 to 2.5 mm with sub-grain diameters ranging from 0.1 to 0.3 mm, with three of five showing evidence of sub-grain development. Thrust fault crystal diameters range from 0.1 to 5 mm with sub-grain diameters ranging from 0.1 to 0.5 mm. Thrust faults contain en echelon tension gashes, shear vein jogs and crenulations.

Microstructures

All fault types exhibit evidence for dynamic recrystallization (Table 1), but it is less evident in strike-slip and thrust faults than in normal faults. Sub-grain development has occurred in all types of faults, and diameters typically range from 0.1 to 0.5 mm. Normal faults show SGR in all samples, which is widely distributed throughout the samples, ±BLG in selected samples. This is not the case for contractional structures, where evidence for dynamic recrystallization is less distributed throughout individual samples. Seven out of 14 strike-slip or thrusting samples show some evidence for SGR and BLG with ±SGR and BLG present in the remaining samples. All samples show both type 1 and 2 calcite twins (Passchier and Trouw 2005; Fossen 2016).

Interpretation

BLG indicates deformation temperatures up to 250°C and SGR suggests temperatures >250°C (Passchier and Trouw 2005). These observations suggest that normal faults experienced higher deformation temperatures than contractional features.

U–Pb calcite geochronology

In total, 21 fault cores have been dated using U–Pb geochronology on calcite slickenfibres and veins. U concentrations range from 0.03 to 2 ppm with >99% of analyses >1 ppm. These are among the

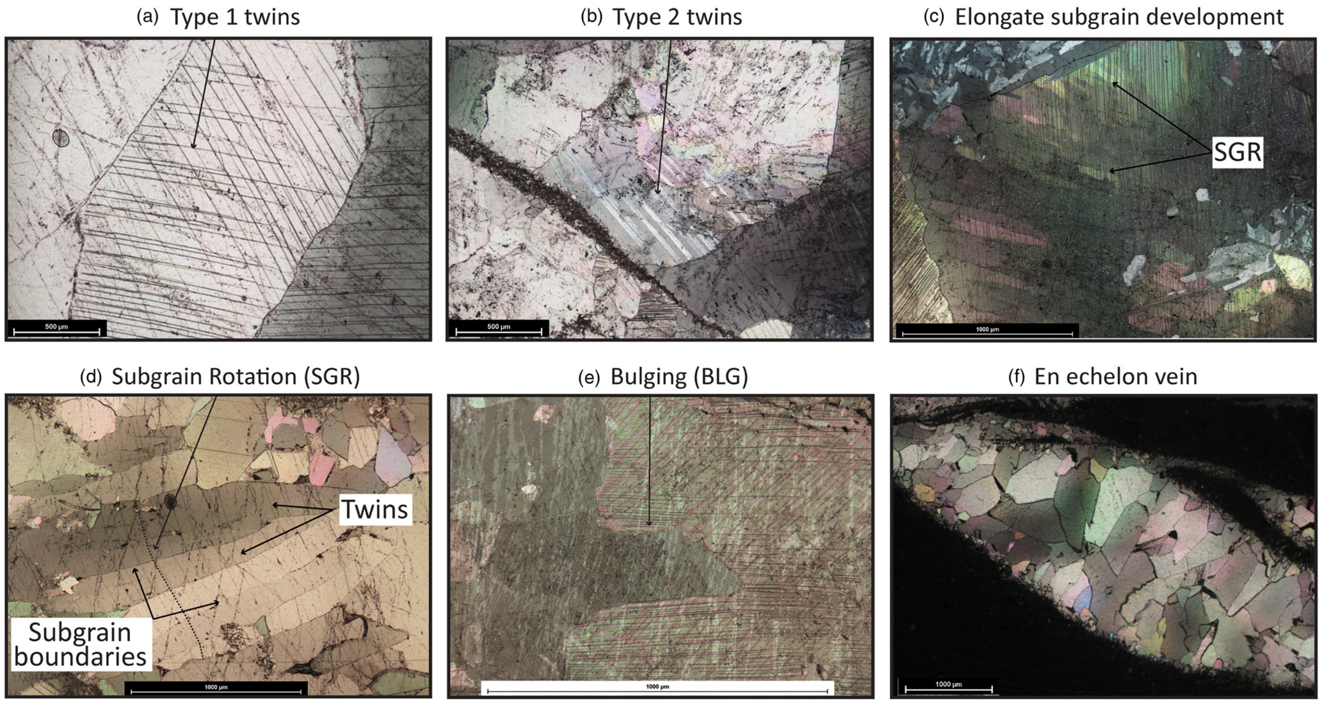

Fig. 5. Texture examples within samples: subgrain rotation (SGR), and bulging (BLG). (**a**) Type 1 twins in JC-8-21. (**b**) Type 2 twins from JC-5-21. (**c**) Elongate subgrain development with minor SGR from JC-3-21 (EQHF). (**d**) SGR picked out by rotation of twins along subgrain boundaries in JC-6b-21. (**e**) BLG between two calcite grains in JC-3-21 (EQHF). (**f**) En echelon vein in JC-4-21.

lowest U concentrations successfully dated for published samples to date. Twenty to 100 U–Pb calcite analyses were performed on each sample (Fig. 6). Samples are relatively radiogenic and have a significant spread in $^{238}U/^{206}Pb$ space (see Supplementary material Table S1). Scatter is relatively minor with MSWDs of 1–3 for all samples using the 86TW plot and regression.

Extensional faults

Seven normal faults were dated and yield a range of ages from *c.* 150.0 ± 2.8 Ma (Kimmeridgian, sample JC-16-21, MSWD = 0.5, *n* = 50) to *c.* 120.2 ± 2.0 Ma (Aptian, sample JC-14-21, MSWD = 1.1, *n* = 45).

Contractional faults

Four samples from sinistral strike-slip fault segments range from 41.0 ± 5.7 Ma (Bartonian, sample JC-1a-21, MSWD = 0.95, *n* = 40) to 34.5 ± 2.5 Ma (Priabonian, sample JC-8-21, MSWD = 0.9, *n* = 40). Four thrust fault segments range from 41.9 ± 1.3 Ma (Bartonian, sample JC-4-21, MSWD = 0.5, *n* = 57) to 36.6 ± 2.6 Ma (Priabonian, sample JC-6B-22, MSWD = 1.00, *n* = 60). Six dextral strike-slip fault segments range from 36.0 ± 1.6 Ma (Priabonian, sample JC-6a-21, MSWD = 1.0, *n* = 39) to 21.8 Ma ± 0.6 (Aquitanian, sample JC-15-21, MSWD = 1.3, *n* = 58).

The East Quantoxhead Fault

A composite vein (sample JC-3-21) from the EQHF has four domains (A–D) that have been dated individually to constrain its temporal structural evolution (Fig. 7). U–Pb ages range from *c.* 147 to *c.* 34 Ma (late Jurassic–Oligocene). Domain A, located at the periphery of the vein, closest to the wall rock yields the oldest age of 147 ± 10 Ma (Tithonian, MSWD = 1.1, *n* = 39). Domains B–C have younger ages, ranging from 136.5 ± 4.3 Ma (Hauterivian, MSWD 3.1 *n* = 20) to 116.5 ± 4.9 Ma (Aptian, MSWD = 3.0, *n* = 20). There are several domains nearer the fault core in which the calcite has a much finer grain size. Celestine occurs as fibrous veins towards the fault core and appears to be spatially associated with the recrystallization of earlier calcite veins. Unfortunately, no age determinations were possible for these recrystallized domains as they did not contain sufficient U. However, the thinnest and finest domain (D) in the fault core was successfully dated and yielded a significantly younger age of 33.5 ± 3.4 Ma (Rupelian, MSWD = 10, *n* = 64).

First-order interpretation of U–Pb calcite ages and textures

Age data show two distinct clusters: normal fault ages range from 150 ± 4 to 120 ± 2.0 Ma whereas strike-slip and thrust fault ages range from 41.9 ± 1.3 to 21.8 ± 0.6 Ma (Fig. 8). The EQHF yields ages that span both these age clusters, suggesting that it has been active for an extended period compared with other individual faults. U–Pb geochronology of the EQHF, combined with microstructural analysis of selected veins, documents the timing of reactivation for the first time (Fig. 7). Vein D yields an age of *c.* 35 Ma, consistent with the range of overlapping ages obtained from strike-slip faults and thrusts in the area (within error).

The structural evolution of the Bristol Channel Basin

Stage 1: north–south Mesozoic extension (*c.* 154–118 Ma)

Both the relative and absolute timing constraints demonstrate that normal faults were the earliest structures to develop within the Bristol Channel Basin (BCB) (Figs 2, 4 and 8). The range of ages obtained from normal faults indicates a protracted period of regional extension during the Late Jurassic and Early Cretaceous (*c.* 154–118 Ma; Fig. 8). Along the southern margin of the BCB, normal faults typically strike east–west (Figs 2 and 3), dipping both to the north and south. The largest faults, for example, the EQHF, Blue Ben Fault and the Kilve Pill Fault (Figs 1 and 4), dip to the south and are broadly synthetic to the Central Bristol Channel Fault Zone (BCFZ), which is interpreted to be a reactivated Variscan thrust (e.g.

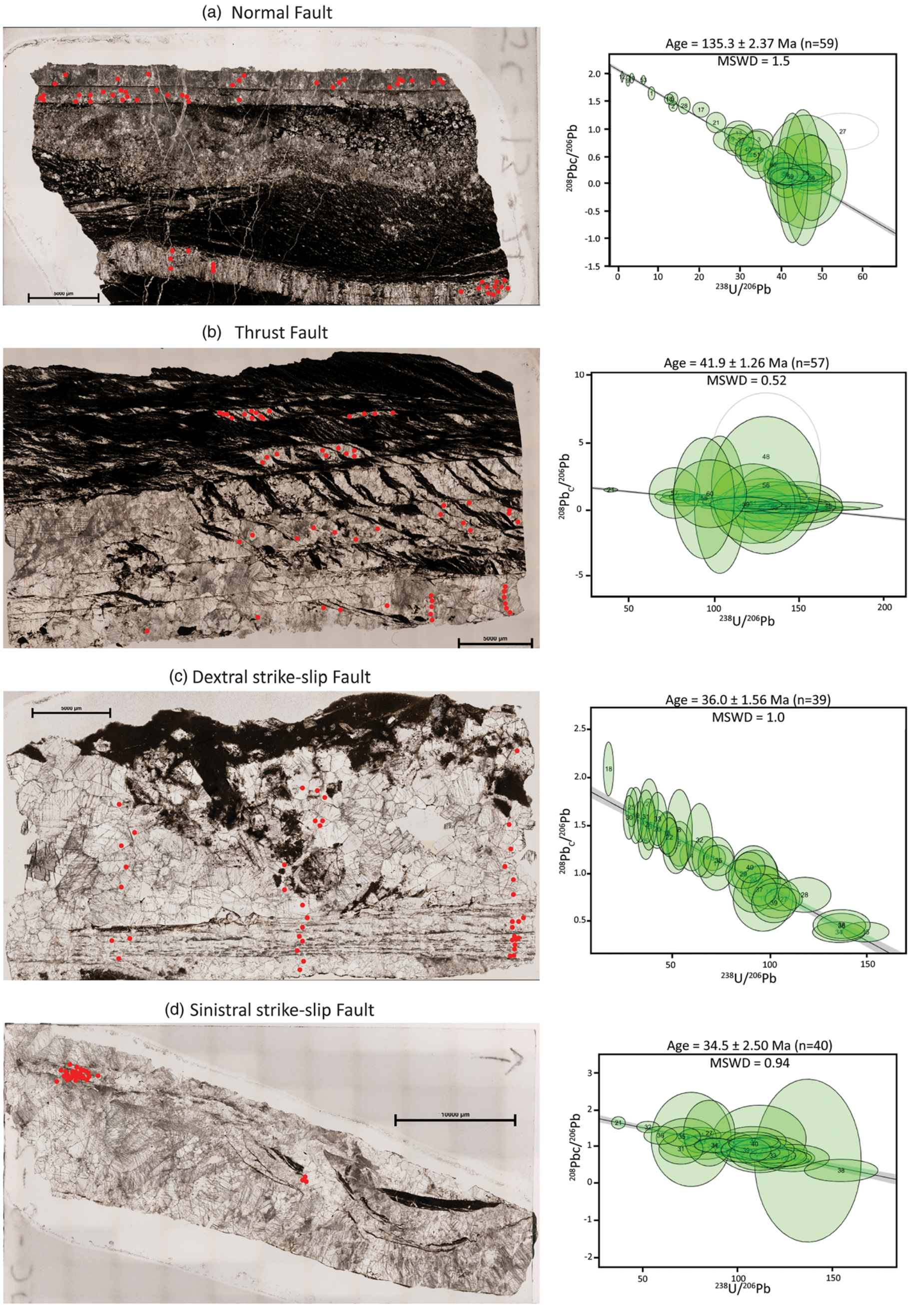

Fig. 6. Representative Tera–Wasserburg plots of different structure types. (**a**) JC-13-21 (normal). 135.3 ± 2.37 Ma (Valanginian), $n = 59$, MSWD = 1.5. (**b**) JC-4-21 (thrust) 41.9 ± 1.26 Ma, $n = 57$, MSWD = 0.52 (Lutetian). (**c**) JC-6a-21 (dextral strike-slip) 36.0 ± 1.56 Ma (Priabonian), $n = 39$, MSWD = 1.0. (**d**) JC-8-21 (sinistral strike-slip). 34.5 ± 2.50 Ma (Priabonian), $n = 40$, MSWD = 0.94.

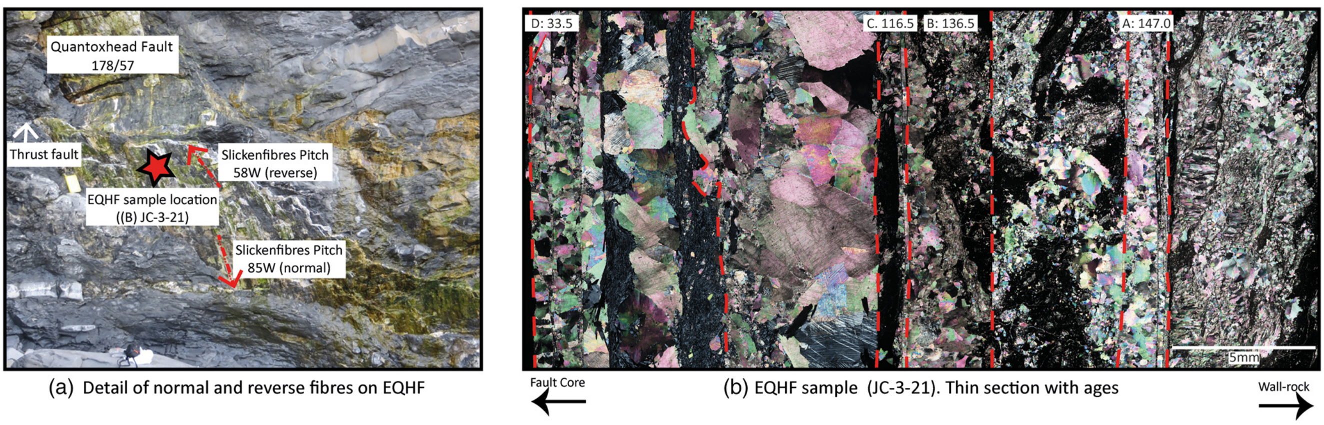

Fig. 7. Sample EQHF (JC-3-21) in thin section, under XPL. Veins A–D have been dated individually, with vein F being located in the fault core of the hanging wall, and A being furthest into the wallrock (hanging wall of the East Quantoxhead Fault). (**a**) Field photograph of EQHF sample location showing reverse and normal fibres. (**b**) Ages acquired from individual veins within the EQHF sample. A: 147.0 ± 10.0 Ma (Tithonian), MSWD 1.1, $n = 39$; B: 136.5 ± 4.26 Ma (Valanginian), MSWD 3.1, $n = 20$; C: 116.5 ± 4.94 Ma (Aptian), MSWD 3.0, $n = 20$; D: 33.5 ± 3.37 Ma (Rupelian), MSWD 10, $n = 64$.

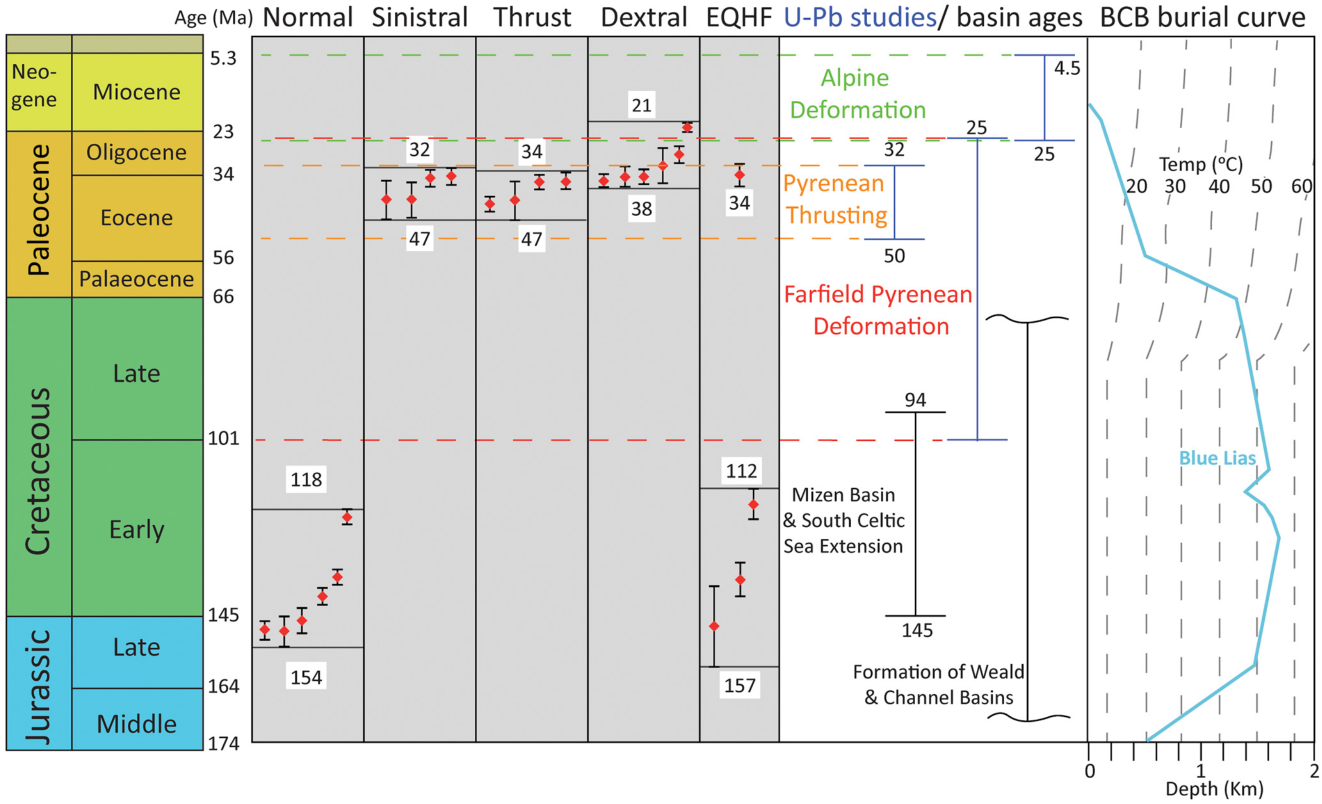

Fig. 8. Summary of age distributions for fault slip types, textures and published U–Pb studies as well as burial curve of the Lias within the BCB. Age ranges extended to ±error range of oldest or youngest fault in population. Normal faults: *c.* 150–120 Ma. Sinistral faults: *c.* 41–35 Ma. Thrust faults: *c.* 42–37 Ma. Dextral faults: *c.* 36–22 Ma. EQHF *c.* 147–116 Ma/34 Ma. Sources: Alpine deformation after Ring and Gerdes (2016) and Looser *et al.* (2021); Pyrenean thrusting after Haines and van der Pluijm (2023); Far-field Pyrenean deformation after Parrish *et al.* (2018), Parizot *et al.* (2020) and Blaise *et al.* (2022); Mizen Basin and South Celtic Sea extension after Rodríguez-Salgado *et al.* (2020); formation of Weald and Channel basins after Lake and Karner (1987); Lias BCB burial curve after Cornford (1986).

Miliorizos 2004). Kinematic analysis of normal faults suggests a broadly NNE–SSW direction of extension (Fig. 3). Locally, where σ_1 axes have more moderate plunges, and normal faults have relatively low angles of dip (<40°), a later tilting of the normal faults, potentially driven by slip on a larger basin bounding fault, is suggested. Peacock *et al.* (2017) suggested that σ_3 within the BCB plunged gently NNE during the Mesozoic, similar to the interpretations presented here.

Extension in the BCB is likely to have been contemporaneous with extension experienced in nearby basins (Figs 8 and 9). The Mizen Basin in the South Celtic Sea is thought to have undergone NW–SE extension from the Berriasian to Hauterivian (*c.* 145–133 Ma) and a later period of north–south extension from the Aptian to Cenomanian (*c.* 125–94 Ma) (Rodríguez-Salgado *et al.* 2020). This later stage of extension is not recorded in the BCB, suggesting that strain may have partitioned away from the BCB by the Late Cretaceous, or later faults are no longer preserved. Age data demonstrate that extension was active in the BCB for a *c.* 30 Myr period, and although kinematic analysis of the fault population (Fig. 3) produces a reliable overall kinematic estimate, there is scatter between faults with up to 45° difference between fault trends. It is therefore possible that these faults developed during slightly different stress regimes over time, potentially driven by a gradual evolution of regional stress, or local stress perturbations as individual structures developed.

Stage 2: Cenozoic thrusting and strike-slip (*c.* 47–21 Ma)

Strike-slip and thrust faults were active during a period of regional contraction from the early Eocene to early Miocene (c. 47–21 Ma). Kinematic analysis of these faults shows that σ_1 remained subhorizontal and broadly north–south throughout contraction (Figs 3 and 8) but that the vertical stress axis flipped between σ_2 and σ_3. Our data do not document a clear progression in stress axis orientation during the transition from regional extension to contraction, as proposed by Peacock *et al.* (2017). Rather, our data indicate that strike-slip and thrust faults formed coevally, within the uncertainties of the dataset, between *c.* 47 and 32 Ma (Fig. 8). Such variability may have resulted from a variety of causes including (1) proximity to major faults, such as the East Quantoxhead Fault (e.g. Fossen 2016), (2) position within relay and transfer zones associated with earlier normal faults (e.g. Rotevatn and Peacock 2018) and (3) slightly different levels of bulk shortening and compartmentalization of strain during contraction (e.g. Butler *et al.* 2006). The BCB system was modelled to have resulted from low maximum shear stress of 10–15 MPa by Stephenson *et al.* (2020). High fluid pressure in the basin would have reduced the effective stress required for failure during inversion (e.g. Williams *et al.* 2005; Holford *et al.* 2008), t**hus reducing the magnitude of stress perturbation required for localized changes in structural style from strike-slip faulting to thrust faulting during contraction.

The contractional episode lasted for a *c.* 30 Myr period and there is significant scatter between faults within the dataset. It is therefore possible that the principal shortening direction did not remain consistent over this period. These data highlight the care needed when conducting kinematic analysis on bulk fault populations as two seemingly related faults used to define one palaeo-kinematic setting may have in fact formed at significantly different times in the geological past.

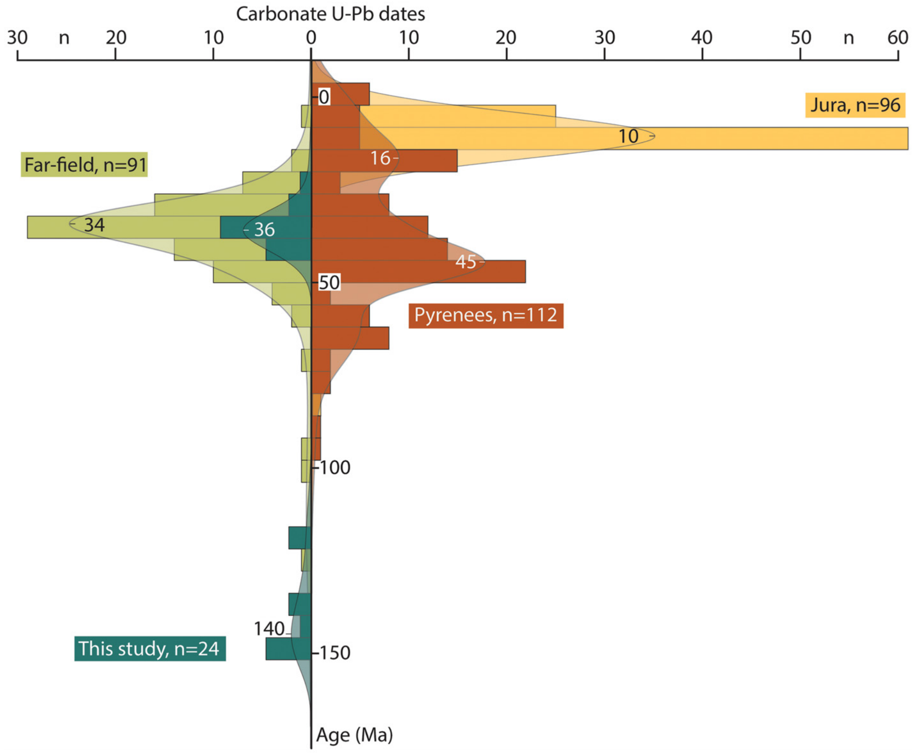

Fig. 9. Kernel density estimation (KDE) plots of new U–Pb calcite ages from the BCB, plotted against U–Pb calcite ages. Full details are given in Supplementary material Table S2. KDE binning = 6 Ma, average uncertainty on dates.Sources: calcite ages from the Pyrenees from Cruset *et al.* (2020), Hoareau *et al.* (2021), Parizot *et al.* (2021), Muñoz-López *et al.* (2022*a*, *b*), Bilau *et al.* (2023) and Haines and van der Pluijm (2023); from the Jura from Looser *et al.* (2021), Smeraglia *et al.* (2021) and Madritsch *et al.* (2024); far-field basin inversion from Parrish *et al.* (2018), Blaise *et al.* (2022) and Monchal *et al.* (2023).

Temperature of deformation

Veins associated with extensional structures show evidence for higher temperature deformation when compared with those associated with contraction structures (Table 1). These observations are in accordance with the burial curve of Cornford (1986) (Fig. 8). The Blue Lias Group, the focus of our study, was at a suggested depth of 1.5–1.7 km and temperature of *c*. 60–70°C during extension. The exhumation path of the burial curve places the same rocks at a depth of 200–400 m and temperature of *c*. 20°C during later contraction. Passchier and Trouw (2005) suggested that temperatures of up to 250°C and above are required to produce SGR, BLG and type 2 twins in calcite. We propose therefore that the protracted nature of deformation, as documented by new age data, coupled with a generally low-strain environment, allowed for the development of these microstructures at lower temperatures (e.g. Kennedy and White 2001; Lacombe 2022).

Fault reactivation

Multiple vein generations developed in the core of the EQHF are evidence for protracted, episodic extension of this structure from the late Jurassic to the later stages of the early Cretaceous (Figs 7 and 8). The structure therefore developed throughout the entire (*c*. 30 Myr) period of extension as defined by the range of ages recorded from individual (unreactivated) normal faults in the area (Figs 7 and 8). This caused the EQHF to become one of the largest faults in the area, making it more prone to reactivation during contraction.

Larger normal faults (>20 m offset) are prone to reactivation, as discussed by Kelly *et al.* (1999). U–Pb geochronology has pinpointed precisely when reactivation occurred. The Blue Ben Fault reactivated at 39 ± 4 Ma via a hanging-wall thrust shortcut (Fig. 2), whereas the fault core of the EQHF underwent direct reactivation and slipped at 34 ± 3 Ma (Fig. 7). All normal faults within the study area, except the EQHF, show evidence for only single slip episodes or they are confined to movement during the extensional phase (stage 1). Reactivation did not seem to occur at the beginning of the contractional phase. It took the EQHF *c*. 15 Myr to reactivate, suggesting that either an extended period of strain accumulation was required to trigger reactivation or the initial contractional stress field inhibited reactivation and favoured the development of strike-slip faulting.

Both contraction and extension were protracted events where strain accumulated in environments with relatively low stress magnitudes (Nemcok and Gayer 1996; Stephenson *et al.* 2020). A high fluid pressure was probably required to reduce both the effective and differential stress acting across faults and formations, allowing fault reactivation (Turner and Williams 2004) and the propagation of new structures.

Regional tectonic framework

The newly constrained period of inversion presented here for the BCB broadly overlaps with widespread basin inversion, which peaked at c. 34 Ma across northern Europe (Figs 8 and 9) (e.g. Parrish *et al.* 2018; Blaise *et al.* 2022; Monchal *et al.* 2023). The cause of this Oligocene and younger basin inversion across Europe remains a matter of debate, with faulting attributed to either late-stage Pyrenean or Alpine deformation. However, the wealth of recent *in situ* carbonate dating studies, where >299 samples have been dated across the Pyrenees, Jura and sedimentary basins across Europe (Fig. 9 and references therein), allows for basin inversion drivers to be put into a direct temporal framework for the first time.

Pyrenean fold and thrust belt development occurred from c. 60 to 20 Ma, where peak deformation, as recorded by carbonate and $^{40}Ar/^{39}Ar$ fault gouge ages, occurred at c. 45 Ma (Cruset *et al.* 2020; Hoareau *et al.* 2021; Parizot *et al.* 2021; Muñoz-López *et al.* 2022*a*, *b*; Bilau *et al.* 2023; Haines and van der Pluijm 2023). Late c. 30–16 Ma faulting in the Pyrenees is attributed to the exhumation of the Pyrenean hinterland (Cruset *et al.* 2020), whereas the main phase of Alpine foreland deformation occurred c. 25–5 Ma (Pfiffner 2002; Sinclair *et al.* 2005). Carbonate U–Pb dating has revealed decoupling of the Alpine Molasse Basin formed faults in the Jura from c. 14 to 4.5 Ma, with a dominant peak c. 10 Ma (Looser *et al.* 2021; Smeraglia *et al.* 2021; Madritsch *et al.* 2024).

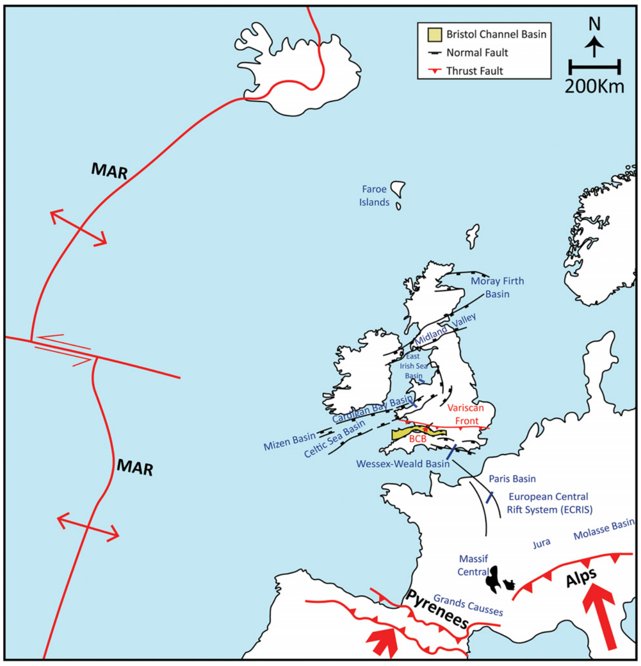

Fig. 10. Bristol Channel Basin in relation to the Pyrenees, Alps and Mid-Atlantic Ridge (MAR). Main direction of transport indicated by arrows. Sources: after Parrish *et al.* (2018); Stephenson *et al.* (2020), Strachan and Woodcock (2020).

The BCB is within the foreland of both the Alpine and Pyrenean orogenic belts, and is also adjacent to the Mid-Atlantic Ridge (Fig. 10). The new age data presented here show that BCB inversion occurred from c. 50 to 20 Ma, with a peak at c. 36 Ma. This exactly fits with the pattern of far-field basin inversion across Europe (Fig. 9) including c. 34 Ma in the Wessex Basin (Parrish *et al.* 2018), c. 48–43 Ma in the Paris Basin (Blaise *et al.* 2022) and during the Eocene in the Irish basins (Monchal *et al.* 2023). These events correlate most closely with post-main phase Pyrenean deformation (Figs 8 and 9) and, when seen as a whole, the compiled European carbonate U–Pb dates demonstrate the significance of Pyrenean deformation for basin inversion across Europe (Fig. 9). We therefore propose that the initial inversion of the BCB was probably driven by the Pyrenean Orogeny. The final stages of BCB inversion from the Oligocene onwards may have been driven by the Alpine Orogeny; however, much younger-aged deformation in the Jura suggests that late-stage exhumation from the Pyrenees may have been a more important driver. Far-field stress modelling conducted by Stephenson *et al.* (2020) showed that significant stress may have also been transmitted to the BCB during the period of inversion from the opening of the Mid-Atlantic Ridge, and it is likely that this event exacerbated the inversion of the BCB. The stress transmitted from these events was unlikely to have been sufficient to cause the basin inversion alone (Williams *et al.* 2005; Holford *et al.* 2009; Stephenson *et al.* 2020).

Conclusions

(1) Structural observations and microtextural analysis have been combined with U–Pb dating to determine absolute timing and kinematic evolution of structures within the Bristol Channel Basin for the first time.

(2) Normal faults displaying consistent normal dip-slip slickenfibres have associated veins that yield ages in the range of *c.* 154–118 Ma and provide absolute age constraints for basin development. These structures exhibit an east–west trend suggesting that there was a protracted *c.* 30 Myr period of north–south extension from the Late Jurassic to Early Cretaceous. These ages can be extrapolated to better constrain the timing of extension of other rift basins in southern Britain, previously mostly dated through relative constraints. These basins include the Mizen Basin in the South Celtic Sea and the Wessex, Weald and Channel basins.

(3) Prominent dextral and sinistral strike-slip faults and localized thrust faults yield ages in the range of *c.* 47–21 Ma. These faults document a period of protracted north–south contraction acting on the basin from the Early Eocene to Early Miocene. Strike-slip and thrust faults formed coevally, suggesting that σ_2 and σ_3 remained similar in magnitude throughout the Eocene–Oligocene, and that minor changes in local confining forces and fluid pressure were able to flip these principal stress axes.

(4) Structures with clear evidence of reactivation (typically >22 m throw) show evidence of multiple fluid infiltration events associated with both normal and reverse slip episodes. In the case of the regionally significant East Quantoxhead Fault, at least three discrete events are recognized. Each texturally distinct vein yields isotopically robust ages ranging from *c.* 150 to 34 Ma.

(5) Cenozoic tectonic inversion of the Bristol Channel Basin occurred during the Eocene–Miocene, contemporaneous with other basins across Europe including the Wessex Basin, Paris Basin, Ireland and the Mizen Basin. Basin inversion was driven by two main tectonic events that caused far-field stresses across Europe, predominantly far-field stresses associated with Pyrenean deformation during the Eocene, with Oligocene–Miocene drivers from Alpine deformation and the opening of the Mid-Atlantic Ridge.

Scientific editing by Pat Meere

Acknowledgements We would like to thank reviewers D. Chew and R. Shail and editor P. Meere for their feedback on the initial submission of the paper. Their comments and advice have thoroughly improved the quality and overall messaging of the paper. We would like to thank D. Peacock for his expert guidance in the field, as well as extensive help with early drafts of the paper. His wealth of knowledge and detailed publications on the region form the scientific foundations on which this project has been built. We would like to thank G. Long, G. Chapman and J. Dunlop for technical assistance at the University of Portsmouth. We would also like to thank W. Andrews at the University of Plymouth, and P. Connolly for valuable advice in structuring the paper in the early stages as well as assistance in the field.

Author contributions **JC**: conceptualization (supporting), data curation (lead), formal analysis (lead), methodology (equal), writing – original draft (lead), writing – review & editing (lead); **MA**: conceptualization (lead), data curation (supporting), formal analysis (supporting), funding acquisition (lead), investigation (equal), methodology (equal), project administration (supporting), resources (supporting), software (supporting), supervision (equal), validation (equal), visualization (equal), writing – original draft (supporting), writing – review & editing (supporting); **CM**: conceptualization (supporting), data curation (equal), formal analysis (equal), funding acquisition (supporting), investigation (equal), methodology (lead), project administration (supporting), resources (equal), software (equal), supervision (equal), validation (equal), visualization (equal), writing – original draft (supporting), writing – review & editing (supporting); **GDP**: data curation (supporting), writing – original draft (supporting), writing – review & editing (supporting); **RP**: formal analysis (supporting), methodology (supporting); **DS**: formal analysis (supporting)

Funding This paper contains work conducted during a PhD study undertaken as part of the Centre for Doctoral Training (CDT) in Geoscience and the Low Carbon Energy Transition. It is sponsored by the University of Plymouth (50%) and NeoEnergy Upstream (50%), whose support is gratefully acknowledged. The U–Pb analyses were undertaken in the Laser Ablation Mass Spectrometry Geochronology laboratory at the University of Portsmouth, and the underpinning financial and technical support is gratefully acknowledged.

Competing interests The authors declare that they have no known competing financial interests or personal relationships that could have appeared to influence the work reported in this paper.

Data availability All data generated or analysed during this study are included in this published article and its supplementary information files.

References

Allmendinger, R.W. 2012. Stratigraphic thickness uncertainty and errors in balanced cross sections. *Geological Society of America, Abstracts with Programs*, **44**, 540.

Barnett-Moore, N., Hassan, R., Flament, N. and Müller, D. 2017. The deep Earth origin of the Iceland plume and its effects on regional surface uplift and subsidence. *Solid Earth*, **8**, 235–254, https://doi.org/10.5194/se-8-235-2017

Bilau, A., Rolland, Y., Dumont, T., Schwartz, S., Godeau, N., Guihou, A. and Deschamps, P. 2023. Early onset of Pyrenean collision (97–90 Ma) evidenced by U–Pb dating on calcite (Provence, SE France). *Terra Nova*, **35**, 413–423, https://doi.org/10.1111/ter.12665

Bixler, W.G., Elmore, R.D. and Engel, M.H. 1998. The origin of magnetization and geochemical alteration in a fault zone, Kilve, England. *Geological Journal*, **33**, 89–105, https://doi.org/10.1002/(SICI)1099-1034(1998040)33:2<89::AID-GJ773>3.0.CO;2-S

Black, L.P. and Gulson, B.L. 1978. The age of the Mud Tank carbonatite, Strangways Range, Northern Territory. *BMR Journal of Australian Geology & Geophysics*, **3**, 227–232.

Blaise, T., Khoudja, S.A.A. *et al.* 2022. Far-field brittle deformation record in the eastern Paris Basin (France). *Geological Magazine*, **159**, 2095–2109, https://doi.org/10.1017/S0016756822000772

Blundell, D.J. 2002. Cenozoic inversion and uplift of southern Britain. *Geological Society, London, Special Publications*, **196**, 85–101, https://doi.org/10.1144/GSL.SP.2002.196.01.06

Boldreel, L.T. and Andersen, M.S. 1993. Late Paleocene to Miocene compression in the Faeroe–Rockall area. *Geological Society, London, Petroleum Geology Conference Series*, **4**, 1025–1034, https://doi.org/10/1144/0041025

Butler, R.W., Tavarnelli, E. and Grasso, M. 2006. Structural inheritance in mountain belts: an Alpine–Apennine perspective. *Journal of Structural Geology*, **28**, 1893–1908, https://doi.org/10.1016/j.jsg.2006.09.006

Chadwick, R.A. 1993. Aspects of basin inversion in southern Britain. *Journal of the Geological Society, London*, **150**, 311–322, https://doi.org/10.1144/gsjgs.150.2.0311

Cohen, K.M., Finney, S.C., Gibbard, P.L. and Fan, J.-X. 2013. The ICS International Chronostratigraphic Chart. *Episodes*, **36**, 199–204, https://doi.org/10.18814/epiiugs/2013/v36i3/002

Coogan, L.A., Parrish, R.R. and Roberts, N.M. 2016. Early hydrothermal carbon uptake by the upper oceanic crust: insight from in situ U–Pb dating. *Geology*, **44**, 147–150, https://doi.org/10.1130/G37212.1

Cornford, C.H.R.I.S. 1986. The Bristol Channel Graben: organic geochemical limits on subsidence and speculation on the origin of inversion. *Proceedings of the Ussher Society*, **6**, 360–367.

Cruset, D., Vergés, J., Albert, R., Gerdes, A., Benedicto, A., Cantarero, I. and Travé, A. 2020. Quantifying deformation processes in the SE Pyrenees using U–Pb dating of fracture-filling calcites. *Journal of the Geological Society, London*, **177**, 1186–1196, https://doi.org/10.1144/jgs2020-014

Dart, C.J., McClay, K. and Hollings, P.N. 1995. 3D analysis of inverted extensional fault systems, southern Bristol Channel basin, UK. *Geological Society, London, Special Publications*, **88**, 393–413, https://doi.org/10.1144/GSL.SP.1995.088.01.21

Debenham, N., Holford, S.P. and King, R.C. 2020. The spatial distribution and geochemical variation of fault and fracture hosted calcite and gypsum cements in the eastern Bristol Channel Basin. *Marine and Petroleum Geology*, **116**, 104320, https://doi.org/10.1016/j.marpetgeo.2020.104320

De Graciansky, P.C., Roberts, D.G. and Tricart, P. 2011. The birth of the Western and Central Alps: subduction, obduction, collision. *In*: De Graciansky, P.C., Roberts, D.G. and Tricart, P. (eds) *Developments in Earth Surface Processes*, **14**. Elsevier, 289–315.

Fossen, H. 2016. *Structural Geology*. Cambridge University Press.

Glen, R.A., Hancock, P.L. and Whittaker, A. 2005. Basin inversion by distributed deformation: the southern margin of the Bristol Channel Basin, England. *Journal of Structural Geology*, **27**, 2113–2134, https://doi.org/10.1016/j.jsg.2005.08.006

Haines, S.H. and van der Pluijm, B.A. 2023. Fault gouge dating in the Spanish Pyrenees: fault ages, thrust propagation sequence, wall-rock provenance, and thermal constraints. *Tectonics*, **42**, e2022TC007251, https://doi.org/10.1029/2022TC007251

Hallam, A. 1971. Mesozoic geology and the opening of the North Atlantic. *Journal of Geology*, **79**, 129–157, https://doi.org/10.1086/627605

Hardman, J.P., Schofield, N. *et al.* 2018. Prolonged dynamic support from the Icelandic plume of the NE Atlantic margin. *Journal of the Geological Society, London*, **175**, 396–410, https://doi.org/10.1144/jgs2017-088

Hestnes, Å., Drost, K. *et al.* 2023. Constraining the tectonic evolution of rifted continental margins by U–Pb calcite dating. *Scientific Reports*, **13**, 7876, https://doi.org/10.1038/s41598-023-34649-z

Hill, C.A., Polyak, V.J., Asmerom, Y. and Provencio, P.P. 2016. Constraints on a Late Cretaceous uplift, denudation, and incision of the Grand Canyon region, southwestern Colorado Plateau, USA, from U–Pb dating of lacustrine limestone. *Tectonics*, **35**, 896–906, https://doi.org/10.1002/2016TC004166

Hoareau, G., Crognier, N. *et al.* 2021. Combination of Δ47 and U–Pb dating in tectonic calcite veins unravel the last pulses related to the Pyrenean shortening (Spain). *Earth and Planetary Science Letters*, **553**, 116636, https://doi.org/10.1016/j.epsl.2020.116636

Holford, S.P., Turner, J.P., Green, P.F. and Hillis, R.R. 2009. Signature of cryptic sedimentary basin inversion revealed by shale compaction data in the Irish Sea, western British Isles. *Tectonics*, **28**, https://doi.org/10.1029/2008TC002359

Huenges, E. 2016. Enhanced geothermal systems: review and status of research and development. *In*: DiPippo, R. (ed.) *Geothermal Power Generation*. Woodhead, 743–761, https://doi.org/10.1016/B978-0-08-100337-4.00025-5

Jackson, S.E., Pearson, N.J., Griffin, W.L. and Belousova, E.A. 2004. The application of laser ablation-inductively coupled plasma-mass spectrometry to in situ U–Pb zircon geochronology. *Chemical Geology*, **211**, 47–69, https://doi.org/10.1016/j.chemgeo.2004.06.017

Jochum, K.P., Stoll, B., Pfänder, J.A., Seufert, M., Flanz, M., Maissenbacher, P., Hofmann, M. and Hofmann, A.W. 2001. Progress in multi-ion counting spark-source mass spectrometry (MIC-SSMS) for the analysis of geological samples. *Fresenius' Journal of Analytical Chemistry*, **370**, 647–653, https://doi.org/10.1007/s002160100786

Jochum, K.P., Weis, U., Stoll, B., Kuzmin, D., Yang, Q., Raczek, I., Jacob, D.E., Stracke, A., Birbaum, K., Frick, D.A. and Günther, D. 2011. Determination of reference values for NIST SRM 610-617 glasses following ISO guidelines. *Geostandards and Geoanalytical Research*, **35**, 397–429, https://doi.org/10.1111/j.1751-908X.2011.00120.x

Kelly, P.G., Sanderson, D.J. and Peacock, D.C.P. 1998. Linkage and evolution of conjugate strike-slip fault zones in limestones of Somerset and Northumbria. *Journal of Structural Geology*, **20**, 1477–1493, https://doi.org/10.1016/S0191-8141(98)00048-0

Kelly, P.G., Peacock, D.C.P., Sanderson, D.J. and McGurk, A.C. 1999. Selective reverse-reactivation of normal faults, and deformation around reverse-reactivated faults in the Mesozoic of the Somerset coast. *Journal of Structural Geology*, **21**, 493–509, https://doi.org/10.1016/S0191-8141(99)00041-3

Kennedy, L.A. and White, J.C. 2001. Low-temperature recrystallization in calcite: mechanisms and consequences. *Geology*, **29**, 1027–1030, https://doi.org/10.1130/0091-7613(2001)029<1027:LTRICM>2.0.CO;2

Lacombe, O. 2022. Calcite Deformation Twins: from crystal plasticity to applications in geosciences. *Geosciences*, **12**, 280, https://doi.org/10.3390/geosciences12070280

Lake, S.D. and Karner, G.D. 1987. The structure and evolution of the Wessex Basin, southern England: an example of inversion tectonics. *Tectonophysics*, **137**, 347–378, https://doi.org/10.1016/0040-1951(87)90328-3

Looser, N., Madritsch, H., Guillong, M., Laurent, O., Wohlwend, S. and Bernasconi, S.M. 2021. Absolute age and temperature constraints on deformation along the basal décollement of the Jura fold-and-thrust belt from carbonate U–Pb dating and clumped isotopes. *Tectonics*, **40**, e2020TC006439, https://doi.org/10.1029/2020TC006439

Lovell, B. 2023. Is the tilt of the Thames valley towards the east caused by a distal lobe of the Icelandic mantle plume? *Proceedings of the Geologists' Association*, **134**, 68–76, https://doi.org/10.1016/j.pgeola.2022.09.002

Madritsch, H., Looser, N., Schneeberger, R., Wohlwend, S., Guillong, M. and Malz, A. 2024. Reconstructing the evolution of foreland fold-and-thrust belts using U–Pb calcite dating: an integrated case-study from the easternmost Jura Mountains (Switzerland). *Tectonics*, **43**, e2023TC008181, https://doi.org/10.1029/2023TC008181

Marrett, R. and Allmendinger, R.W. 1990. Kinematic analysis of fault-slip data. *Journal of Structural Geology*, **12**, 973–986, https://doi.org/10.1016/0191-8141(90)90093-E

Miliorizos, M., Ruffell, A. and Brooks, M. 2004. Variscan structure of the inner Bristol Channel, UK. *Journal of the Geological Society, London*, **161**, 31–44, https://doi.org/10.1144/0016-764903-035

Monchal, V., Drost, K. and Chew, D. 2023. Precise U–Pb dating of incremental calcite slickenfiber growth: evidence for far-field Eocene fold reactivation in Ireland. *Geology*, **51**, 611–615, https://doi.org/10.1130/G50906.1

Mottram, C.M., Kellett, D.A., Barresi, T., Zwingmann, H., Friend, M., Todd, A. and Percival, J.B. 2020. Syncing fault rock clocks: direct comparison of U–Pb carbonate and K–Ar illite fault dating methods. *Geology*, **48**, 1179–1183, https://doi.org/10.1130/G47778.1

Muñoz-López, D., Cruset, D. *et al.* 2022*a*. U–Pb dating and geochemical dataset of fracture-filling calcite veins from the Bóixols–Sant Corneli anticline (Southern Pyrenees). *Data in Brief*, **45**, 108636, https://doi.org/10.1016/j.dib.2022.108636

Muñoz-López, D., Cruset, D. *et al.* 2022*b*. Spatio-temporal variation of fluid flow behavior along a fold: the Bóixols–Sant Corneli anticline (Southern Pyrenees) from U–Pb dating and structural, petrographic and geochemical constraints. *Marine and Petroleum Geology*, **143**, 105788, https://doi.org/10.1016/j.marpetgeo.2022.105788

Nemcok, M. and Gayer, R. 1996. Modelling palaeostress magnitude and age in extensional basins: a case study from the Mesozoic Bristol Channel Basin, UK. *Journal of Structural Geology*, **18**, 1301–1314, https://doi.org/10.1016/S0191-8141(96)00048-X

Nemčok, M., Gayer, R. and Miliorizos, M. 1995. Structural analysis of the inverted Bristol Channel Basin: implications for the geometry and timing of fracture porosity. *Geological Society, London, Special Publications*, **88**, 355–392, https://doi.org/10.1144/GSL.SP.1995.088.01.20

Parizot, O., Missenard, Y. *et al.* 2020. Tectonic record of deformation in intraplate domains: case study of far-field deformation in the Grands Causses Area, France. *Geofluids*, **2020**, 1–19, https://doi.org/10.1155/2020/7598137

Parizot, O., Missenard, Y., Haurine, F., Blaise, T., Barbarand, J., Benedicto, A. and Sarda, P. 2021. When did the Pyrenean shortening end? Insight from U–Pb geochronology of syn-faulting calcite (Corbières area, France). *Terra Nova*, **33**, 551–559, https://doi.org/10.1111/ter.12547

Parrish, R.R., Parrish, C.M. and Lasalle, S. 2018. Vein calcite dating reveals Pyrenean orogen as cause of Paleogene deformation in southern England. *Journal of the Geological Society, London*, **175**, 425–442, https://doi.org/10.1144/jgs2017-107

Passchier, C.W. and Trouw, R.A. 2005. *Microtectonics*. Springer.

Paton, C., Hellstrom, J., Paul, B., Woodhead, J. and Hergt, J. 2011. Iolite: freeware for the visualisation and processing of mass spectrometric data. *Journal of Analytical Atomic Spectrometry*, **26**, 2508–2518, https://doi.org/10.1039/c1ja10172b

Peacock, D.C.P. 2009. A review of Alpine deformation and stresses in southern England. *Italian Journal of Geosciences*, **128**, 307–316, https://doi.org/10.3301/IJG.2009.128.2.307

Peacock, D.C.P. and Sanderson, D.J. 1991. Displacements, segment linkage and relay ramps in normal fault zones. *Journal of Structural Geology*, **13**, 721–733, https://doi.org/10.1016/0191-8141(91)90033-F

Peacock, D.C.P. and Sanderson, D.J. 1993. Estimating strain from fault slip using a line sample. *Journal of Structural Geology*, **15**, 1513–1516, https://doi.org/10.1016/0191-8141(93)90011-X

Peacock, D.C.P. and Sanderson, D.J. 1999. Deformation history and basin-controlling faults in the Mesozoic sedimentary rocks of the Somerset coast. *Proceedings of the Geologists' Association*, **110**, 41–52, https://doi.org/10.1016/S0016-7878(99)80005-4

Peacock, D.C., Tavarnelli, E. and Anderson, M.W. 2017. Interplay between stress permutations and overpressure to cause strike-slip faulting during tectonic inversion. *Terra Nova*, **29**, 61–70, https://doi.org/10.1111/ter.12249

Pfiffner, O.A., Schlunegger, F. and Buiter, S.J.H. 2002. The Swiss Alps and their peripheral foreland basin: stratigraphic response to deep crustal processes. *Tectonics*, **21**, 3-1–3-16, https://doi.org/10.1029/2000TC900039

Philipp, S.L. 2012. Fluid overpressure estimates from the aspect ratios of mineral veins. *Tectonophysics*, **581**, 35–47, https://doi.org/10.1016/j.tecto.2012.01.015

Ring, U. and Gerdes, A. 2016. Kinematics of the Alpenrhein–Bodensee graben system in the Central Alps: Oligocene/Miocene transtension due to formation of the Western Alps arc. *Tectonics*, **35**, 1367–1391, https://doi.org/10.1002/2015TC004085

Roberts, N.M. and Holdsworth, R.E. 2022. Timescales of faulting through calcite geochronology: a review. *Journal of Structural Geology*, **158**, 104578, https://doi.org/10.1016/j.jsg.2022.104578

Roberts, N.M. and Walker, R.J. 2016. U–Pb geochronology of calcite-mineralized faults: absolute timing of rift-related fault events on the northeast Atlantic margin. *Geology*, **44**, 531–534, https://doi.org/10.1130/G37868.1

Roberts, N.M., Rasbury, E.T., Parrish, R.R., Smith, C.J., Horstwood, M.S. and Condon, D.J. 2017. A calcite reference material for LA-ICP-MS U–Pb geochronology. *Geochemistry, Geophysics, Geosystems*, **18**, 2807–2814, https://doi.org/10.1002/2016GC006784

Roberts, N.M., Drost, K. *et al.* 2020. Laser ablation inductively coupled plasma mass spectrometry (LA-ICP-MS) U–Pb carbonate geochronology: strategies, progress, and limitations. *Geochronology*, **2**, 33–61, https://doi.org/10.5194/gchron-2-33-2020

Rodríguez-Salgado, P., Childs, C., Shannon, P.M. and Walsh, J.J. 2020. Structural evolution and the partitioning of deformation during basin growth and inversion: a case study from the Mizen Basin Celtic Sea, offshore Ireland. *Basin Research*, **32**, 830–853, https://doi.org/10.1111/bre.12402

Rotevatn, A. and Peacock, D.C. 2018. Strike-slip reactivation of segmented normal faults: implications for basin structure and fluid flow. *Basin Research*, **30**, 1264–1279, https://doi.org/10.1111/bre.12303

Rowley, E. and White, N. 1998. Inverse modelling of extension and denudation in the East Irish Sea and surrounding areas. *Earth and Planetary Science Letters*, **161**, 57–71, https://doi.org/10.1016/S0012-821X(98)00137-X

Sanderson, D.J. 2016. Field-based structural studies as analogues to sub-surface reservoirs. *Geological Society, London, Special Publications*, **436**, 207–217, https://doi.org/10.1144/SP436.5

Sinclair, H.D., Gibson, M., Naylor, M. and Morris, R.G. 2005. Asymmetric growth of the Pyrenees revealed through measurement and modeling of orogenic fluxes. *American Journal of Science*, **305**, 369–406, https://doi.org/10.2475/ajs.305.5.369

Smeraglia, L., Looser, N., Fabbri, O., Choulet, F., Guillong, M. and Bernasconi, S.M. 2021. U–Pb dating of middle Eocene–Pliocene multiple tectonic pulses in the Alpine foreland. *Solid Earth*, **12**, 2539–2551, https://doi.org/10.5194/se-12-2539-2021

Spruženiece, L., Späth, M., Urai, J.L., Ukar, E., Selzer, M. and Nestler, B. 2021. Wide-blocky veins explained by dependency of crystal growth rate on fracture surface type: insights from phase-field modeling. *Geology*, **49**, 641–646, https://doi.org/10.1130/G48472.1

Stephenson, R., Schiffer, C., Peace, A., Nielsen, S.B. and Jess, S. 2020. Late Cretaceous–Cenozoic basin inversion and palaeostress fields in the North Atlantic–western Alpine–Tethys realm: implications for intraplate tectonics. *Earth-Science Reviews*, **210**, 103252, https://doi.org/10.1016/j.earscirev.2020.103252

Stewart, M., Strachan, R.A. and Holdsworth, R.E. 1999. Structure and early kinematic history of the Great Glen Fault Zone, Scotland. *Tectonics*, **18**, 326–342, https://doi.org/10.1029/1998TC900033

Strachan, R. and Woodcock, N.H. 2020. The tectonic pattern of Britain and Ireland. In *Encyclopedia of Geology*. Elsevier, 328–337, https://doi.org/10.1016/B978-0-12-409548-9.12412-1

Tamas, A., Holdsworth, R.E. *et al.* 2022. New onshore insights into the role of structural inheritance during Mesozoic opening of the Inner Moray Firth Basin, Scotland. *Journal of the Geological Society, London*, **179**, https://doi.org/10.1144/jgs2021-066

Tiley, R., White, N. and Al-Kindi, S. 2004. Linking Paleogene denudation and magmatic underplating beneath the British Isles. *Geological Magazine*, **141**, 345–351, https://doi.org/10.1017/S0016756804009197

Torfstein, A. and Steinberg, J. 2020. The Oligo-Miocene closure of the Tethys Ocean and evolution of the proto-Mediterranean Sea. *Scientific Reports*, **10**, 13817, https://doi.org/10.1038/s41598-020-70652-4

Turner, J.P. and Williams, G.A. 2004. Sedimentary basin inversion and intra-plate shortening. *Earth-Science Reviews*, **65**, 277–304, https://doi.org/10.1016/j.earscirev.2003.10.002

Vergés, J., Fernàndez, M. and Martìnez, A. 2002. The Pyrenean orogen: pre-, syn-, and post-collisional evolution. *Journal of the Virtual Explorer*, **8**, 55–74, https://doi.org/10.3809/jvirtex.2002.00058

Vermeesch, P. 2018. IsoplotR: a free and open toolbox for geochronology. *Geoscience Frontiers*, **9**, 1479–1493, https://doi.org/10.1016/j.gsf.2018.04.001

Williams, G.A., Turner, J.P. and Holford, S.P. 2005. Inversion and exhumation of the St George's Channel basin, shttps://doi.org/10.1144/0016-764904-023

Williams, G.D., Powell, C.M. and Cooper, M.A. 1989. Geometry and kinematics of inversion tectonics. *Geological Society, London, Special Publications*, **44**, 3–15, https://doi.org/10.1144/GSL.SP.1989.044.01.02

Zhang, L., Huang, H., Wang, Y., Ren, B., Ren, S., Chen, G. and Zhang, H. 2014. CO_2 storage safety and leakage monitoring in the CCS demonstration project of Jilin oilfield, China. *Greenhouse Gases: Science and Technology*, **4**, 425–439, https://doi.org/10.1002/ghg.1411